Early diagnosis of gastric cancer based on deep learning combined with the spectral-spatial classification method

YUANPENG LI,[1,2] LIANGYU DENG,[1] XINHAO YANG,[1] ZHAO LIU,[3] XIAOPING ZHAO,[3] FURONG HUANG,[1,4] SIQI ZHU,[1] XINGDAN CHEN,[1] ZHENQIANG CHEN,[1,5] AND WEIMIN ZHANG[3,6]

[1]*Guangdong Provincial Key Laboratory of Optical Fiber Sensing and Communications, Department of Optoelectronic Engineering, Jinan University, Guangdong, Guangzhou, 510632, China*
[2]*College of physical science and technology, Guangxi Normal University, Guangxi, Guilin, 541004, China*
[3]*Department of Gastroenterology and Endocrinology, The 74th Group Army Hospital of People's Liberation Army, Guangdong, Guangzhou, 510318, China*
[4]*furong_huang@163.com*
[5]*tzqchen@jnu.edu.cn*
[6]*weigert@163.com*

Abstract: The development of an objective and rapid method that can be used for the early diagnosis of gastric cancer has important clinical application value. In this study, the fluorescence hyperspectral imaging technique was used to acquire fluorescence spectral images. Deep learning combined with spectral-spatial classification methods based on 120 fresh tissues samples that had a confirmed diagnosis by histopathological examinations was used to automatically identify and extract the "spectral + spatial" features to construct an early diagnosis model of gastric cancer. The model results showed that the overall accuracy for the nonprecancerous lesion, precancerous lesion, and gastric cancer groups was 96.5% with specificities of 96.0%, 97.3%, and 96.7% and sensitivities of 97.0%, 96.3%, and 96.6%, respectively. Therefore, the proposed method can increase the diagnostic accuracy and is expected to be a new method for the early diagnosis of gastric cancer.

1.   Introduction

Gastric cancer (GC) is one of the common malignancies that originate from epithelial cells on the gastric mucosa. According to global data, GC is the fourth most common malignancy in the world and the second leading cause of cancer-related deaths [1]. The occurrence and development of GC are complicated and affected by multiple factors such as environment and heredity, and the influence of these factors on the occurrence of GC has not been fully elucidated. The five-year survival rate of advanced GC is still lower than 30% even after the comprehensive treatment of surgery, chemotherapy, and radiotherapy [2], while the five-year survival rate after the treatment of early GC can be more than 90%, even reaching the cure effect [3]. Therefore, early diagnosis of GC is very important.

The occurrence and development of GC is a complex process of multistage, multistep, and multiple mechanisms. There are a series of intermediate stages (including the precancerous state). At present, the more recognized pattern of human GC was proposed by Correa [4]: "normal gastric mucosa - chronic non-atrophic gastritis - atrophic gastritis - intestinal metaplasia - dysplasia - gastric cancer." The diseases of atrophic gastritis (AG) and intestinal metaplasia (IM) are considered to be precancerous lesions that are highly associated with GC [5]. AG and IM have a greater risk of developing into GC if not treated in time. Their early detection and timely treatment have important practical significance for the prevention and treatment of GC.

At present, there are various methods for the early diagnosis of GC, including endoscopic diagnosis [general endoscopy, endoscopic ultrasonography, magnifying endoscopy, chromoendoscopy (CE), etc.] [6–9], histopathological diagnosis [10], imaging diagnosis (X-ray examination, computed tomography examination, nuclear magnetic resonance, etc.) [11–13], and tumor marker diagnosis (pepsinogen, gastrin 17, GC markers, etc.) [14–17]. However, these diagnostic methods still have the following shortcomings: the endoscopic diagnosis method is subjective and easy to miss, histopathological diagnosis requires invasive examination and time-consuming and analytical procedures that require specialized knowledge and training, and the imaging diagnosis method cannot effectively diagnose early lesions. Tumor markers are mostly used to evaluate the therapeutic effect of GC, but there is still no effective tumor marker for GC [18–21]. Therefore, an objective, rapid, and accurate method for the early diagnosis of GC should be developed.

Fluorescence hyperspectral imaging (FHSI) technology can be used to obtain the spatial image information and spectral information of samples, which makes it possible to perform spectral analysis on all pixel regions of the space, Therefore, it can realize the functions that cannot be directly achieved by traditional optical imaging and the spectral method. This method can detect some physiological and pathological changes of biological tissues through its spectral features. N. Bedard et al. found that when excited with blue light, normal tissue emits a pale blue/green autofluorescence while dysplastic and cancerous regions with reduced autofluorescence appear dark-brown [22]. Besides, this method can establish a more elaborate model for the early diagnosis of some diseases through its "spatial + spectral" features [23,24]. G. Lu et al. [25] proved that the spectral-spatial classification method can obtain better classification results than the traditional spectral classification and spatial classification methods [26,27].

Because spectral classification utilizes only the spectral features of a single pixel, the spatial relationship of adjacent pixels is ignored. Spatial classification is limited to image spatial information in a certain spectral band and ignores the information of the composition of the material provided by the spectrum. To improve the interpretation and classification ability of hyperspectral data, it is necessary to integrate spatial and spectral information in the low-dimensional space through a spectral-spatial classification method.

In addition, hyperspectral images contain rich high-dimensional data. Owing to the limitations of manually extracting features by using traditional machine learning algorithms (decision tree, random forest, and support vector machine), it is impossible to learn representative feature representations from these high-dimensional data. A solution to the problem of gradient disappearance in deep network training was proposed by Hiton et al. [28] in 2006: "unsupervised training initialization of weights + fine-tuning of supervised training" which provides an effective solution for deep learning. AlexNet, a deep learning network was built by the Hiton team in 2012, has made a major breakthrough in the field of image recognition, and made deep learning become one of the current research hotspots [29,30]. Hierarchical feature representations can be automatically learned from existing data by using the deep learning method, which can overcome the limitations of manually extracted features.

At present, deep learning has been widely reported in the field of medical image analysis. Ma et al. [31] combined hyperspectral imaging with convolutional neural networks (CNNs) for the identification of normal and head and neck cancer tissues, and achieved an accuracy of 91.36%. Levin [32] published a paper in Lancet Respiratory Medicine in which lung CT images were combined with deep convolutional neural networks. He found that this can accurately assess pulmonary fibrosis with an accuracy of 95%. Byrne et al. [33] employed narrow-band imaging combined with a CNN for the identification of small colon polyps (adenomas and hyperplastic polyps) and found that the accuracy was 94%. Wang et al. [34] employed two-dimensional shear-wave elastography combined with a CNN to assess the stage of hepatic fibrosis and achieved an accuracy of above 95%. However, the application of FHSI combined with deep learning in the early diagnosis of GC has not been reported.

In view of the wealth of information available about FHSI and the biochemical complexity of tumor development, in this paper, a modeling method based on deep learning combined with the spectral-spatial classification method is proposed for fluorescence hyperspectral images. This method uses the entire spectrum of each pixel and the information from its neighborhood to build the model. This is applied to the early diagnosis of GC to provide an objective, rapid, and accurate diagnostic method for the early diagnosis of GC.

2. Materials and methods

2.1. Experiment equipment and image acquisition

In this experiment, an FHSI system designed and built by the Department of Optoelectronic Engineering at Jinan University was used. The core components included an ultraviolet xenon light source with a central wavelength of 361 nm and its interference filter, a liquid-crystal tunable filter (LCTF, CRI Inc., VariSpec VIS, Connecticut City, United States) useful for narrow-band filtering within the 400-720 nm range, a 16-bit complementary metal-oxide semiconductor (CMOS, Hamamatsu Inc., Hamamatsu City, Japan), a dichroic mirror with a cutoff wavelength of 425 nm (Thorlabs Inc., New Jersey City, United States) that can separate laser light, and a signal light. The system also contains a lens set, video capture card, and computer. Figure 1 shows the FHSI system.
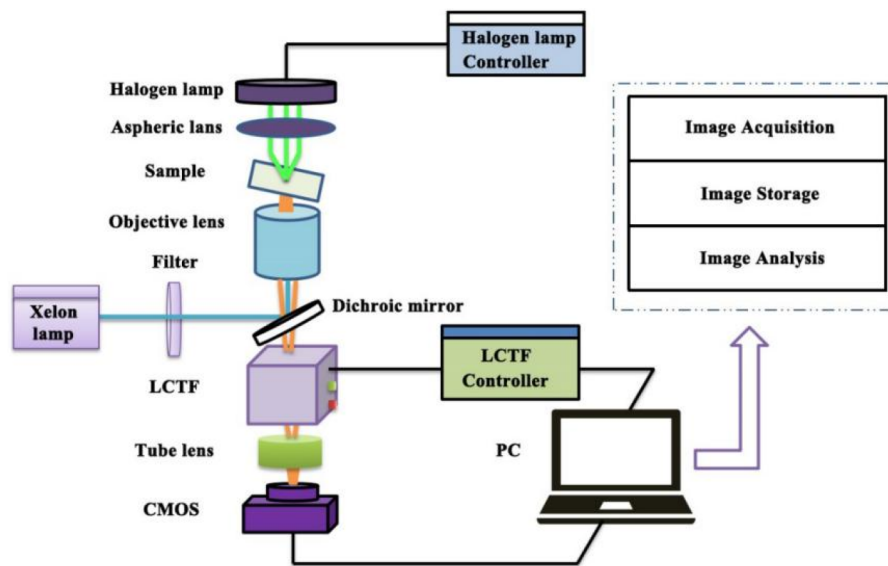

Fig. 1. Fluorescence hyperspectral imaging system.

Spectral cube acquisition: The sample was placed on a slide. The microscope was adjusted at low magnification (5×) until a clear image could be seen. Following that, a 361 nm ultraviolet laser was used for fluorescence emission, and one image frame was acquired at every 2 nm interval in the 450-680 nm range. In total, 116 fluorescence spectral images were acquired for each patient (experiment temperature: 25 ± 1 °C, humidity: 46% relative humidity).

The large network model and parameters in a convolutional neural network (CNN) require a large amount of internal memory and computing resources during the training phase, and has higher requirements for the computing platform. The main advantage of GPU over CPU is the parallel computing capability, thus reducing the training time, and we constructed a relevant hardware platform to solve the problem of high-speed calculations by selecting a suitable graphics

processing unit (GPU).The specific information of the computing platform is as follows: CPU: Intel Core i5-8500, base frequency: 3 GHz, GPU: NVIDIA chip, GTX1080Ti motherboard, 11-GB GDDR5 memory with 3584 stream processing units, internal memory: 16-GB DDR4 RECC internal memory, power supply: Jetsoft 600 W, and motherboard: Gigabyte Z270 HD3.

All data preprocessing was performed using our open-source SIproc software, implemented in C++ and CUDA. Training and testing were performed in Python using open-source software packages. TensorFlow, which leveraged the TFlearn interface, was used to design and implement CNNs.

2.2. Experimental samples

The fresh gastric mucosal tissues used in this study were obtained from the Departments of Gastroenterology at the People's Liberation Army 74th Group Army Hospital and Zhujiang Hospital of Southern Medical University. There were 120 patients: 62 male and 58 female. The mean age was 55 years. Among these samples, there were 53 cases with nonprecancerous lesions (including normal gastric tissue and nonatrophic gastritis), 35 cases with precancerous lesions (AG accompanied by IM), and 32 cases with GC. Other pathological types were excluded.

During gastroscopic examination, conventional disposable biopsy forceps (tip width of 6 mm) were used. Two adjacent tissue-sample blocks of apparent lesions were collected. One block was used for histopathological diagnosis, while the other was not treated but placed inside a cryovial and immediately stored in a liquid nitrogen tank. The time interval from tissue sample collection to spectral image detection was 1 week. All samples were operated by endoscopists with five or more years of experience, and diagnoses were made by pathologists with eight or more years of experience. Informed consent was obtained from patients for the collection of gastric mucosal tissue samples. This process conformed to ethical requirements, and the patients were informed of the situation.

2.3. ResNet

The residual network (ResNet) was proposed by Kaiming He [35] et al. in 2015. Compared with the classic CNN architecture, ResNet's main feature is the introduction of residual connectivity, which can solve its performance degradation problem when training a very deep network [36,37]. At present, a large number of ResNet-based works have been proposed and successfully applied to different fields such as natural language processing [38], speech recognition [39,40], and remote sensing image classification [41]. The application of ResNet has also improved the performance of the corresponding models.

In general, a deep residual network consists of a set of residual blocks, each containing several stacked convolutional layers [with a modified linear unit (ReLU) and a batch-normalized layer attached as a convolutional layer]. A residual block with an identity map can be expressed as Eq. (1).

$$h_{l+1} = Relu(h_l + F(h_l, w_l)) \tag{1}$$

where h_l and h_{l+1} are the input and output of the first residual block, respectively; Relu(.) is rectified linear unit function; F is the residual mapping function; and ω_l is the parameter of the residual learning unit. Specifically, when the channel (size) of $F(h_l, \omega_l)$ and h_l are not equal, a linear projection is usually applied to match the size, so Eq. (1) can be further converted to Eq. (2).

$$\mathrm{h}_{l+1} = Relu(\varphi(h_l) + F(h_l, w_l)) \tag{2}$$

The Resnet34 framework was built in this paper and is shown in Fig. 2. A basic residual block is shown in Fig. 2(B). Figure 2(A) shows a 34-layer plain network, and Fig. 2(B) shows a 34-layer residual network. Compared with the plain network, the residual network has a shortcut that directly implements the direct connection route of the unit map, similar to a "short circuit."

Through experiments, this structure with a shortcut can effectively solve the problem of gradient disappearance.
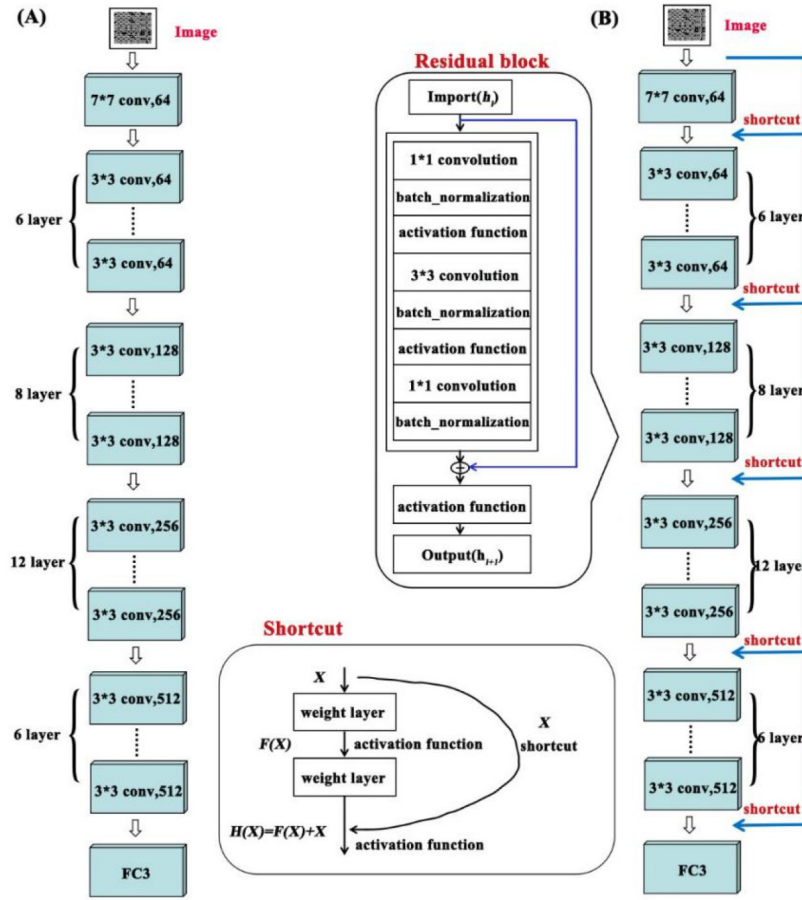

Fig. 2. Schematic diagram of residual network

2.4.   Assessment of model parameters

During the construction of the CNN diagnosis model, the accuracy, loss function threshold, specificity, and sensitivity are important assessment markers. The closer the accuracy, specificity, and sensitivity are to 1, the better the diagnosis results of the constructed model. Equations (3)–(5) show the formulas for the different parameters.

$$Accuracy = \frac{n_{correct}}{n_{total}} \tag{3}$$

$$Loss = NLL(W, b) = -\sum_{i=1}^{|Y|} \log Y(i) \tag{4}$$

$$\text{TPR} = \frac{TP}{TP + FN} \tag{5}$$

$$FPR = \frac{TN}{FP + TN}$$

In Eq. (5), *TPR* represents the sensitivity, *FPR* represents the specificity, *TP* represents the number of positive samples from the validation set that were correctly classified by the model, *FN* represents the number of positive samples from the validation set that were wrongly classified by the model, *FP* represents the number of negative samples from the validation set that were wrongly classified by the model, and *TN* represents the number of negative samples from the validation set that were correctly classified by the model.

3. Results

3.1. Fluorescence spectra analysis

3.1.1. Spectral acquisition and normalization

Each sample was detected by an FHSI system to obtain a spectral cube consisting of 116 frames of 256-order grayscale images. Figure 3(A) is a fluorescence image of a gastric mucosal tissue sample at a peak of 608 nm (normal, AG, IM, GC). A binary image is shown in Fig. 3(B). The spectral curve of the gastric tissue is drawn by randomly selecting 100 pixels from the spectral cube. The normalized spectra of normal, AG, IM, and GC are shown in Fig. 3(C).
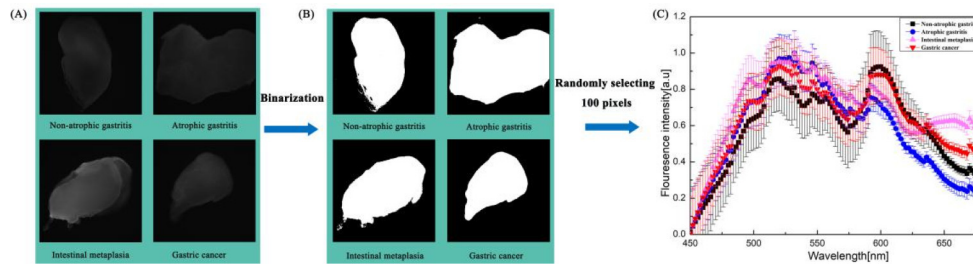

Fig. 3. Schematic diagram of spectral acquisition: (A) original fluorescence image; (B) binarized image; and (C) average spectrum by normalization of each tissue.

3.1.2. Original spectral analysis

Human tissue autofluorescence groups are listed in Table 1 [42]. The average spectra of normal, AG, IM, and GC are shown in Fig. 4. The error bars in Fig. 4(A) represent the difference in fluorescence intensity between different pixel points. In Fig. 4(B), 496 nm is the fluorescent characteristic peak of the pyridoxal phosphate "Schiff" base, 546 nm is the fluorescent characteristic peak of phospholipid, and 670 nm is the fluorescent characteristic peak of hematoporphyrin. The fluorescence intensity of normal gastric mucosa at 496 nm was weaker than that of the lesion, indicating that the metabolic abnormality of the pyridoxal phosphate "Schiff" base was accompanied by lesions. The fluorescence intensity of normal gastric mucosa and AG at 546 nm and 670 nm was stronger than that of IM and GC, indicating that gastric mucosa is accompanied by an abnormal metabolism of phospholipids during carcinogenesis. In addition, the fluorescence intensity of IM and GC were relatively close, indicating that the intestinal epithelial metaplasia is similar to the tissue fluorescent substance composition of GC. This also indicates that IM has a greater risk of canceration.

3.1.3. Second derivative spectral analysis

In this study, gastric mucosal tissue samples were divided into three groups: nonprecancerous lesion group, precancerous lesion group, and gastric adenocarcinoma group. Figure 5(A) shows the second derivative spectrum of the nonprecancerous lesion group, precancerous lesion group, and GC group. The value of 466 nm is a hydrophobic subunit ubiquinone reductase (NADPH).
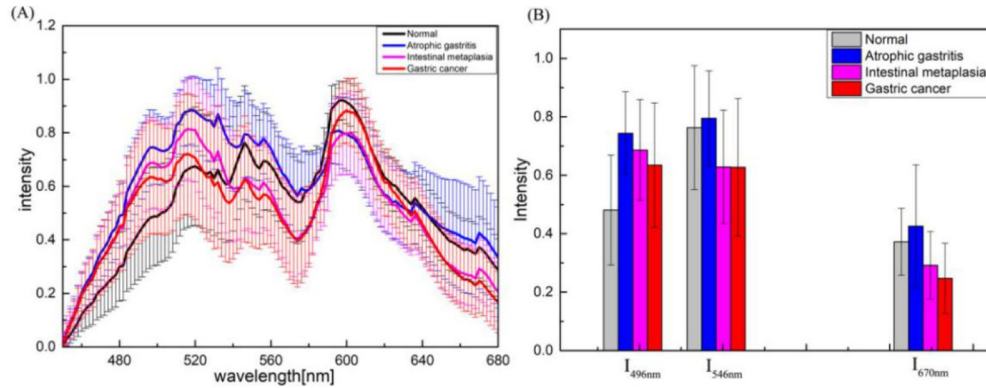
Fig. 4. Average spectrum of normal, atrophic gastritis, intestinal metaplasia, and gastric cancer: (A) average spectrum of each tissue with error bars and (B) average spectral intensity of each tissue at 496 nm, 546 nm, and 670 nm.

Table 1. Autofluorescence groups, excitation wavelengths, and emission wavelengths of human tissue components.

Endogenous fluorescent substance	Biological component	Autofluorescence excitation/emission
Aromatic amino acid	Functional protein	(240-280 nm) / (280-350 nm)
Cytokeratin	Intracellular fibrin	(280-325 nm) / (495-525 nm)
Collagen, elastin	Extracellular protein fiber	(350-420 nm) / (420-510 nm)
Riboflavin	Coenzyme of key enzymes in redox reactions	(330-380 nm) / (440, 462 nm)
Hydrophobic subunit ubiquinone reductase	Coenzyme of key enzymes in redox reactions	(350-370nm) / (480, 540 nm)
fatty acid	Lipid accumulation	(330-350 nm) / (470-480 nm)
Vitamin A/Vitamin B6	Carotenoid/pyridoxal phosphate "Schiff" base	(370-380 nm) / (490-510 nm)
Protoporphyrin IX and porphyrin derivatives	Protein (apolipoprotein) repair group	(405 nm) / (630-700 nm)
Lipofuscin	Mixed (protein, lipid, vitamin a)	(UV, 400-500 nm) / (480-700 nm)
Lecithin	Cell membrane main component	(436 nm) / (540 nm, 560 nm)

The intensity of NADPH in the GC group is significantly lower than that in the nonprecancerous lesion group and the precancerous lesion group and may be caused by abnormal NADPH metabolism in GC tissues. The value of 546 nm is a phospholipid in the body lipid, and the intensity of phospholipids in the GC group is significantly greater than that in the nonprecancerous lesion group and the precancerous lesion group. Phospholipids are the main component of the cell membrane and may be caused by an abnormal phospholipid metabolism in the cell membrane of the GC group. The error bars in Fig. 5(B) represent the difference in fluorescence intensity between different individuals.
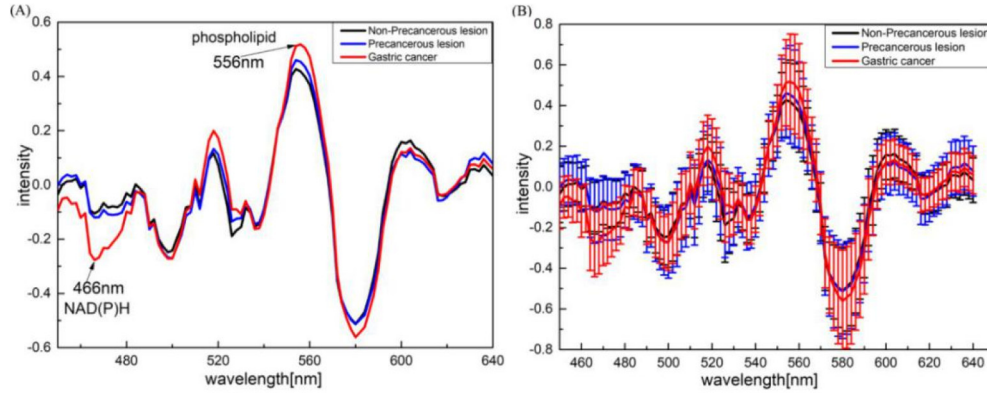

Fig. 5. Second-derivative spectra of nonprecancerous lesions, precancerous lesions, and gastric cancer: (A) average spectrum of second derivative and (B) average spectrum of second-derivative with error bars.

3.2. ResNet34 model

3.2.1. Spatiospectral preprocessing

A spectral cube was obtained after acquiring every sample by the spectral imaging system. This cube was composed of images from 116 frames and 256 grayscale levels. First, the region of the target image (size: 200×200) was extracted. Following that, 10×10 pixels were used to form a $10 \times 10 \times 100$-long one-dimensional vector in 100 consecutive wave bands, which was converted to a 100×100 two-dimensional matrix. This step was traversed across the entire image to obtain a series of 400 two-dimensional matrix images containing spatial-spectral information. Figure 6 shows the procedure of spatial-spectral preprocessing. Images of nonprecancerous lesions, precancerous lesions, and GC are shown in Fig. 7. Case and picture information of nonprecancerous lesion group, precancerous lesion group, and gastric cancer group are shown in Table 2.

Table 2. Case and picture information of nonprecancerous lesion group, precancerous lesion group, and gastric cancer group.

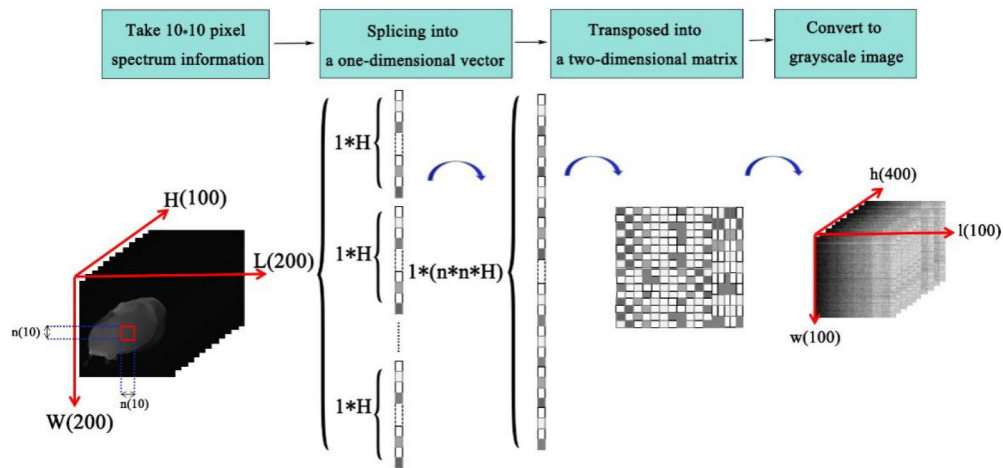| Grouping of observations	non-precancerous lesions group	precancerous lesions group	gastric cancer group	total
Number of cases	53	35	32	120
Original fluorescent image/picture	53×100	35×100	32×100	12000
Image of spatial-spectral/pictue	53×400	35×400	32×400	48000

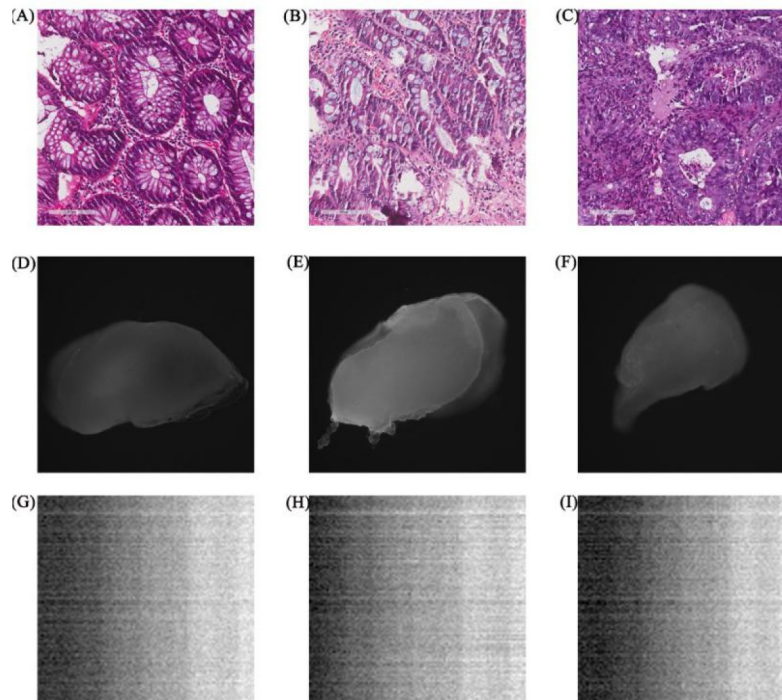**Fig. 6.** Schematic diagram of spatiospectral preprocessing.

Fig. 7. Image of nonprecancerous lesions, precancerous lesions, and gastric cancer: Figs.7(A)–(C) histopathological image; Figs.7(D)–(F) original fluorescent image; and Figs.7(G)–(I) spatiospectral image.

3.2.2. Sample set division

A sample set division of spatiospectral images is listed in Table 3. The ResNet34 model randomly selects the joint spatial-spectral preprocessed images in a 3:1:1 ratio for the training set (28,800 images), validation set (9600 images), and test set (9600 images).

Table 3. Sample set division of spatiospectral image.

Sample set	non-precancerous lesions group	precancerous lesions group	gastric cancer group	total
training set	12720	8400	7680	28800
Validation set	4240	2800	2560	9600
test set	4240	2800	2560	9600

3.2.3. Structure framework of ResNet34

In this study, hyperspectral image data characteristics and classification requirements were used to design ResNet34. This study is a multiple classification of the problems of the nonprecancerous lesion, precancerous lesion, and GC groups. Figure 8 shows the entire framework. Figure 8(A) shows a spatiospectral image; (B) contains one convolutional layer and four residual blocks, where depth feature extraction is carried out to extract the features of the middle convolution layer and obtain the feature expression by mean pooling; and (C) shows a softmax multiclass classification, which outputs the category information for I (nonprecancerous lesion group), II (precancerous lesion group), and III (GC group).
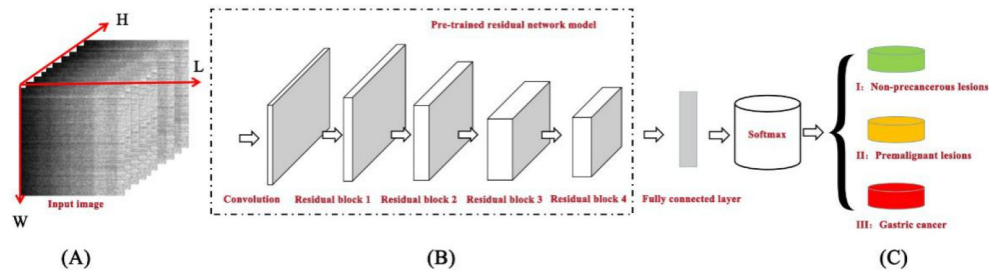

Fig. 8. Schematic diagram of Resnet34 for early diagnosis of gastric cancer: (A) image dataset by using spatiospectral preprocessing; (B) convolutional layer and residual module; and (C) fully connected layer and softmax multiclassifier.

3.2.4. Result of ResNet34 model

The results of 200 iterations of the ResNet34 model are shown in Fig. 9. As shown in Fig. 9(A), the accuracy of the training set and the validation set are not much different when the number of iterations is within 0-18. After the number of iterations is greater than 18, the accuracy of the training set is significantly higher than that of the validation set. The accuracy of the training set and the validation set constantly increase with an increase in the iteration times when the number of iterations is within 0-40, and the accuracy gradually stabilizes after the number of iterations is higher than 40.

As shown in Fig. 9(B), the thresholds of the loss function in the training set and the validation set are not much different when the number of iterations is within 0-14. After the number of iterations is greater than 14, the thresholds of the loss function in the training set are significantly smaller than those of the validation set. The thresholds of the loss function in the training set and the validation set are constantly reduced with an increase in the iteration times when the
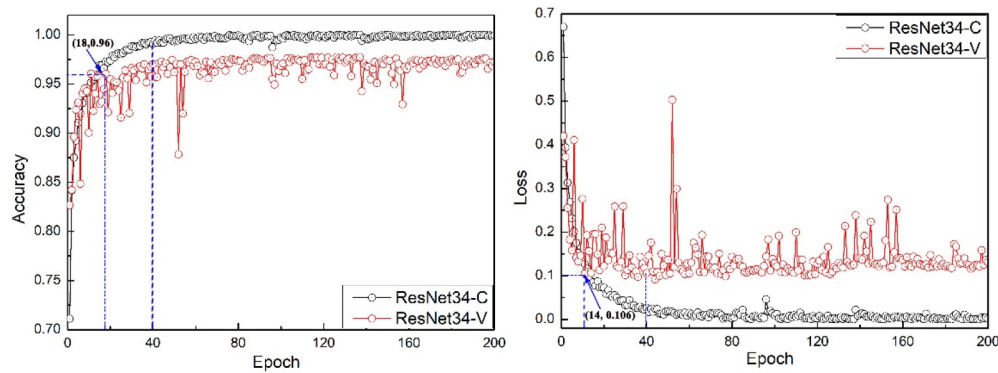
Fig. 9. Modeling results of Resnet34: (A) accuracy rate varies with number of iterations and (B) curve of loss function varies with number of iterations.

number of iterations is within 0-40, and the threshold of the loss function gradually stabilizes after the number of iterations is higher than 40. As can be seen from the results, the results of the ResNet34 model vary greatly with changes in the number of iterations (learning times). The best results are as follows: the accuracy rate of the training set is 99.8%, the threshold of the loss function is 0.009, the accuracy rate of the validation set is 97.30%, and the threshold of the loss function is 0.79.

3.3. Superparameter optimization and prediction results

To further optimize the model, we optimized the batch size, momentum factor, number of iterations, and learning rate for ResNet34. The parameter optimization settings were as follows: batch size (10-100, step length: 1); momentum factor (0-0.9, step length: 0.1); learning rate (0.0001, 0.001, 0.01, [0.1-0.7, step length 0.1]), and the maximum number of iterations was 200. Gradual optimization was carried out for these four parameters. The optimization results are shown in Fig. 10. Optimal results were obtained when the batch size was 10, the momentum factor was 0.2, the learning rate was 0.6, the number of iterations was 126, and the accuracy of the validation set was 97.72%.

Optimized parameters (batch size = 10, momentum factor = 0.2, learning rate = 0.6, and number of iterations = 126) were used to construct the ResNet34 model. Figure 10 shows the operation results. The weight parameters in the trained model were used to predict the samples in the test set. Table 4 lists the results of the test set: the overall accuracy was 96.5%, and the specificities of the nonprecancerous lesion, precancerous lesion, and GC groups were 96.0%, 97.3%, and 96.7%, respectively. The sensitivities were 97.0%, 96.3%, and 96.6%, respectively.

Table 4. Results of Resnet34 model for test set.

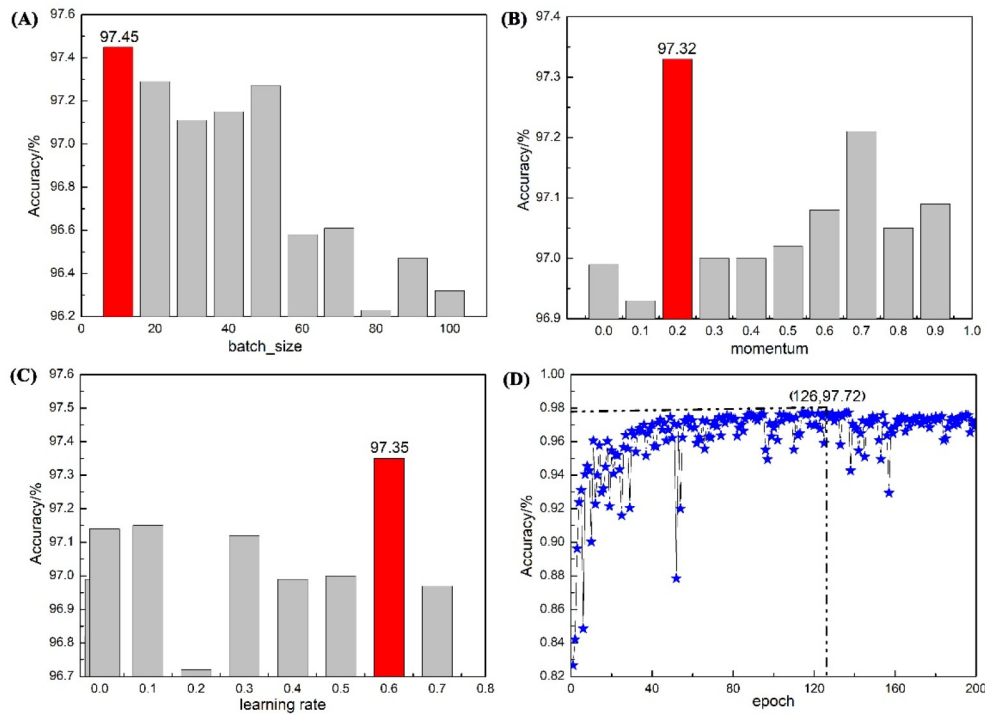| True value	Predicted value		
	non-precancerous lesions group	precancerous lesions group	gastric cancer group
non-precancerous lesions group	4070	80	90
precancerous lesions group	41	2724	35
gastric cancer group	59	28	2473
specificity/%	96.0	97.3	96.7
sensitivity/%	97.0	96.2	96.5

Fig. 10. Model hyperparameter optimization results.

4. Discussion

The error bars shown in Fig. 3(D) represent the spectral differences of different spatial parts of the gastric mucosa of the same individual. The spatial distribution of the constituents of the fluorescent substance is not uniform, resulting in a large difference in the fluorescence intensity between the pixels. In addition, the spatial difference in the spectral intensity varies with the wavelength range. For example, nonprecancerous lesions have large spatial differences before the 600 nm band, while spatial differences after 600 nm are small. There will be differences between different types of tissues. In the range of error fluctuations, the fluorescence intensity of normal tissues overlaps with the fluorescence intensity of other types of tissues (AG, IM, and GC). Therefore, 496 nm as a spectral fingerprint of normal and disease, and 546 nm and 670 nm as differential fingerprints of GC and nongastric cancer, respectively, are more likely to produce misjudgments.

The error bars shown in Fig. 5(B) represent the differences between different individuals in the same category. It can be seen from Fig. 5(B) that the second derivative spectrum is greatly affected by individual differences, and the fluorescence intensity of each tissue type at 550 nm and 580 nm overlaps more severely, indicating that the individual differences in these two bands are larger. The fluorescence intensity of the tissue types at 466 nm and 546 nm also partially overlap, and this may cause significant interference in the identification of nonprecancerous lesions, precancerous lesions, and GC. Therefore, it is easy to misjudge GC and nongastric cancer when only using the 466 nm and 546 nm values of the second derivative spectrum.

In summary, it is necessary to further use fluorescence spectroscopy imaging technology combined with deep learning and the spatial-spectral combined classification method in modeling diagnoses. This will allow for the extraction of more effective information for the nonprecancerous

lesion group, precancerous lesion group, and GC group samples. Perform reliable and accurate identification.

Because biological tissues are so complex, it is likely that many biomolecular components are involved in countless biochemical processes that simultaneously affect disease. Deep learning combined with the spectral-spatial classification method can be used for multiple pathological classification and to make full use of "spatial + spectral" information. In this experiment, the accuracy of nonprecancerous lesions, precancerous lesions, and GC reached 96.5% by using this method, indicating that deep learning combined with the spectral-spatial classification method is effective and reliable for the early diagnosis of GC.

The accuracy rate is relatively high when using the deep learning method and as the result of the difference in gray image information after spatiospectral preprocessing. The information of the fluorescence component in different bands and the spatial difference information of the fluorescence component at different pixel points was included in the image after spatiospectral preprocessing. The difference information of "spatial + spectral" for these grayscale images could be automatically learned by using the deep learning method, and the advanced feature representation was obtained. Finally, the accurate category information of each type of tissue was output (including the nonprecancerous group, precancerous lesion group, and GC group).

Early GC diagnosis has always been a local and overseas research hotspot. As shown in Table 5, new endoscopic techniques [chromoendoscopy (CE), narrow-band imaging (NBI), blue laser imaging (BLI), and optical coherence tomography (OCT)], new tumor markers (mRNA), spectral detection [infrared spectral (IR) and Raman spectrum (RS)], the identification of small and high-risk nonneoplastic gastric lesions (e.g., AG and IM), and GC have made certain progress. However, the accuracy of the endoscopic method mainly depends on the clinician's experience. The specificity and sensitivity of tumor markers have not reached the requirements of clinical application. The infrared spectrum of water has a great influence on other substances, which causes significant interference to some lesion information in the early stage of GC and is easily covered up by the water absorption signal. Owing to the weakness of Raman scattering, a large confocal Raman spectrometer is required to meet the measurement requirements in the laboratory. In addition, chemical reagents such as special metal nanomaterials are needed for surface-enhanced Raman spectroscopy analysis. Thus, Raman spectroscopy is difficult to popularize and apply in clinical practice.

Table 5. Comparison of early diagnosis effect (accuracy, specificity, and sensitivity) of gastric cancer based on different methods.

Sequence Number	Detection method	accuracy/%	specificity/%	sensitivity/%
1	Chromoendoscopy (CE) [43]	91.3	88.6	93.2
2	Narrow-band imaging (NBI) [44]	93.6	92.7	94.5
3	Blue laser imaging (BLI) [45]	92.1	93.8	91.6
4	Optical coherence imaging (OCT) [46]	90.7	91.7	88.2
5	mRNA(h19) [47]	82.8	85.5	80.1
6	Infrared spectral (IR) [48]	89.2	84.0	94.0
7	Raman spectrum (RS) [49]	92.0	95.0	78.0
8	Fluorescence hyperspectral imaging (FHSI)	96.5	97.3	96.2

According to the existing literature, here, we presented for the first time the application of FHSI combined with a deep learning algorithm (ResNet34) and spectral-spatial classification method as a sensitive and specific diagnostic tool for the early diagnosis of GC. A good classification of nonprecancerous lesions, precancerous lesions, and GC was obtained. This indicates the feasibility of using FHSI technology for the early diagnosis of GC. FHSI technology can

simultaneously obtain the biochemical information and image spatial information of gastric mucosa tissue, and has great clinical application potential.

Conclusions

The fluorescence spectrum characteristics of GC tissues are significantly different from those of normal tissues. This may be caused by the abnormal metabolism of the pyridoxal phosphate "Schiff" base concentration and hematoporphyrin IX concentration. In addition, the fluorescence intensity of a GC group in the second-derivative spectrum was significantly lower than that of the nonprecancerous and precancerous groups. This may be caused by the abnormal NADPH metabolism in the GC tissues. These endogenous fluorescence substances can be used as spectral biomarkers to distinguish nonprecancerous lesions, precancerous lesions, and GC. However, owing to the great influence of the spatial distribution differences of tissue components, individual differences, and instrument noise, the fluorescence spectra overlap is significant and is easy to misjudge. The discrimination accuracy, specificity, and sensitivity of a deep learning model for the nonprecancerous lesion group, precancerous lesion group, and GC group were all above 96%, and the stability of the model was effectively improved by adjusting the superparameters through experience.

Disclosures

The authors declare that there are no conflicts of interest related to this article.

References

1. F. Bray, J. Ferlay, I. Soerjomataram, R. L. Siegel, L. A. Torre, and A. Jemal, "Global Cancer Statistics 2018: GLOBOCAN Estimates of Incidence and Mortality Worldwide for 36 Cancers in 185 Countries," Ca-Cancer J. Clin. **68**(6), 394–424 (2018).
2. K. D. Miller, R. L. Siegel, C. C. Lin, A. B. Mariotto, J. L. Kramer, J. H. Rowland, K. D. Stein, R. Alteri, and A. Jemal, "Cancer Treatment and Survivorship Statistics, 2016," Ca-Cancer J. Clin. **66**(4), 271–289 (2016).
3. H. Katai, T. Ishikawa, K. Akazawa, Y. Isobe, I. Miyashiro, I. Oda, S. Tsujitani, H. Ono, S. Tanabe, T. Fukagawa, S. Nunobe, Y. Kakeji, and A. Nashimoto, "Five-year survival analysis of surgically resected gastric cancer cases in Japan: a retrospective analysis of more than 100,000 patients from the nationwide registry of the Japanese Gastric Cancer Association(2001-2007)," Gastric Cancer **21**(1), 144–154 (2018).
4. P. Correa and M. B. Piazuelo, "Natural history of helicobacter pylori infection," Dig. Liver Dis. **40**(7), 490–496 (2008).
5. Y. H. Park and N. Kim, "Review of atrophic gastritis and intestinal metaplasia as a premalignant lesion of gastric cancer," J. Cancer Prev. **20**(1), 25–40 (2015).
6. R. S. van der Post, J. V. Dieren, A. Grelack, N. Hoogerbrugge, L. E. van der Kolk, P. Snaebjornsson, I. L. Vogelaar, J. H. van Krieken, T. M. Bisseling, and A. Cats, "Outcomes of screening gastroscopy in first-degree relatives of patients fulfilling hereditary diffuse gastric cancer criteria," Gastrointest. Endosc. **87**(2), 397–404.e2 (2018).

7. R. P. Merkow, G. Herrera, D. A. Goldman, H. G. Mark, A. S. Arnold, J. M. Vivian, E. S. Murray, F. B. Daniel, and G. Coit, "Endoscopic Ultrasound as a Pretreatment Clinical Staging Tool for Gastric Cancer: Association with Pathology and Outcome," Ann. Surg. Oncol. **24**(12), 3658–3666 (2017).

8. H. Doyama, N. Yoshida, S. Tsuyama, R. Ota, Y. Takeda, H. Nakanishi, K. Tsuji, K. Tominaga, S. Tsuji, K. Takemura, S. Yamada, K. Katayanagi, H. Kurumaya, A. Iwashita, and K. Yao, "The "white globe appearance" (WGA): a novel marker for a correct diagnosis of early gastric cancer by magnifying endoscopy with narrow-band imaging (M-NBI)," Gastrointest. Endosc. **3**(2), E120–E124 (2015).

9. R. Hüneburg, T. Marwitz, P. van Heteren, T. J. Weismüller, J. Trebicka, R. Adam, S. Aretz, A. P. Bouza, D. Pantelis, J. C. Kalff, J. Nattermann, and C. P. Strassburg, "Chromoendoscopy in combination with random biopsies does not improve detection of gastric cancer foci in CDH1 mutation positive patients," Gastrointest. Endosc. **4**(12), E1305–E1310 (2016).

10. M. Plummer, E. Buiatti, G. Lopez, S. Peraza, J. Vivas, W. Oliver, and N. Munoz, "Histological diagnosis of precancerous lesions of the stomach: a reliability study," Int. J. Epidemiol. **26**(4), 716–720 (1997).

11. T. Gotoda, H. Ishikawa, H. Ohnishi, K. Sugano, C. Kusano, C. Yokoi, Y. Matsuyama, and F. Moriyasu, "Randomized controlled trial comparing gastric cancer screening by gastrointestinal X-ray with serology for Helicobacter pylori and pepsinogens followed by Gastrointest. Endosc.," Gastric Cancer **18**(3), 605–611 (2015).

12. T. Saito, Y. Kurokawa, S. Takiguchi, Y. Miyazaki, T. Takahashi, M. Yamasaki, H. Miyata, K. Nakajima, M. Mori, and Y. Doki, "Accuracy of multidetector-row CT in diagnosing lymph node metastasis in patients with gastric cancer," Eur. Radiol. **25**(2), 368–374 (2015).

13. A. W. Chan, P. Mercier, D. Schiller, R. Bailey, S. Robbins, D. T. Eurich, M. B. Sawyer, and D. Broadhurst, "1H-NMR urinary metabolomic profiling for diagnosis of gastric cancer," Br. J. Cancer **114**(1), 59–62 (2016).

14. H. Watabe, T. Mitsushima, Y. Yamaji, R. W. Okamoto, T. Kokubo, H. Doi, H. Yoshida, T. Kawabe, and M. Omata, "Predicting the development of gastric cancer from combining Helicobacter pylori antibodies and serum pepsinogen status: a prospective endoscopic cohort study," Gut **54**(6), 764–768 (2005).

15. M. J. Duffy, R. Lamerz, C. Haglund, A. Nicolini, M. Kalousová, L. Holubec, and C. Sturgeon, "Tumor markers in colorectal cancer, gastric cancer and gastrointestinal stromal cancers: European group on tumor markers 2014 guidelines update," Int. J. Cancer **134**(11), 2513–2522 (2014).

16. Q. Li, Y. Shao, X. Zhang, T. Zheng, M. Miao, L. Qin, B. Wang, G. Ye, B. Xiao, and J. Guo, "Plasma long noncoding RNA protected by exosomes as a potential stable biomarker for gastric cancer," Tumor Biol. **36**(3), 2007–2012 (2015).

17. Y. Shao, M. Ye, X. Jiang, W. Sun, X. Ding, Z. Liu, G. Ye, X. Zhang, B. Xiao, and J. Guo, "Gastric juice long noncoding RNA used as a tumor marker for screening gastric cancer," Cancer **120**(21), 3320–3328 (2014).

18. H. Xue, A. Yang, F. Liu, X. Sun, and X. Liu, "Clinical significance of Serum Pepsinogen I/II and gastrin-17 determination in gastric cancer diagnosis and prognosis," Eur. J. Inflammation **16**, 1–4 (2018).

19. M. J. Duffy, R. Lamerz, C. Haglund, A. Nicolini, M. Kalousová, L. Holubec, and C. Sturgeon, "Tumor markers in colorectal cancer, gastric cancer and gastrointestinal stromal cancers: European group on tumor markers 2014 guidelines update," Int. J. Cancer **134**(11), 2513–2522 (2014).

20. P. Li, S. Chen, H. Chen, X. Mo, T. Li, Y. Shao, B. Xiao, and J. Guo, "Using circular RNA as a novel type of biomarker in the screening of gastric cancer," Clin. Chim. Acta **444**, 132–136 (2015).

21. X. Zhou, C. Yin, Y. Dang, F. Ye, and G. Zhang, "Identification of the long non-coding RNA H19 in plasma as a novel biomarker for diagnosis of gastric cancer," Sci. Rep. **5**(1), 11516 (2015).

22. N. Bedard, R. A. Schwarz, A. Hu, V. Bhattar, J. Howe, M. D. Williams, A. M. Gillenwater, R. R. Kortum, and T. S. Tkaczyk, "Multimodal snapshot spectral imaging for oral cancer diagnostics: a pilot study," Biomed. Opt. Express **4**(6), 938–949 (2013).

23. C. Balas, V. Papadakis, N. Papadakis, A. Papadakis, E. Vazgiouraki, and G. Themelis, "A novel hyper-spectral imaging apparatus for the non-destructive analysis of objects of artistic and historic value," J. Cult. Herit. **4**(Suppl. 1), 330–337 (2003).

24. A. Picon, O. Ghita, P. F. Whelan, and P. M. Iriondo, "Fuzzy spectral and spatial feature integration for classification of nonferrous materials in hyperspectral data," IEEE Trans. Ind. Inf. **5**(4), 483–494 (2009).

25. G. Lu and B. Fei, "Medical hyperspectral imaging: a review," J. Biomed. Opt. **19**(1), 010901 (2014).

26. L. Yang, S. Yang, and R. Zhang, "Semi-Supervised Hyperspectral Image Classification Using Spatio-Spectral Laplacian Support Vector Machine," IEEE Geosci. Remote Sensing Lett. **11**(3), 651–655 (2014).

27. J. Li, J. M. Bioucas-Dias, and A. Plaza, "Spectral-Spatial Classification of Hyperspectral Data Using Loopy Belief Propagation and Active Learning," IEEE Trans. Geosci. Remote Sensing **51**(2), 844–856 (2013).

28. G. E. Hinton and R. R. Salakhutdinov, "Reducing the dimensionality of data with neural networks," Science **313**(5786), 504–507 (2006).

29. A. Krizhevsky, I. Sutskever, and G. E. Hinton, "ImageNet Classification with Deep Convolutional Neural Networks," *Advances in Neural Information Processing Systems*, 1–9 (2012).

30. Y. Lecun, Y. Bengio, and G. Hinton, "Deep learning," Nature **521**(7553), 436–444 (2015).

31. L. Ma, G. Lu, D. Wang, X. Wang, Z. G. Chen, S. Muller, A. Chen, and B. Fei, "Deep learning based classification for head and neck cancer detection with hyperspectral imaging in an animal model," SPIE Medical Imaging **137**, 101372G (2017).

32. D. L. Levin. "Deep learning and the evaluation of pulmonary fibrosis," *The Lancet Respiratory Medicine*. https://doi.org/10.1016/S2213-2600(18)30371-0(2018).

33. M. F. Byrne, N. Chapados, F. Soudan, C. Oertel, M. L. Pérez, R. Kelly, N. Iqbal, F. Chandelier, and D. K. Rex, "Real-time differentiation of adenomatous and hyperplastic diminutive colorectal polyps during analysis of unaltered videos of standard colonoscopy using a deep learning model," Gut **68**(1), 94–100 (2019).

34. K. Wang, X. Lu, H. Zhou, Y. Gao, J. Zheng, M. Tong, C. Wu, C. Liu, L. Huang, T. Jiang, F. Meng, Y. Lu, H. Ai, X. Y. Xie, L. Yin, P. Liang, J. Tian, and R. Zheng, "Deep learning Radiomics of shear wave elastography significantly improved diagnostic performance for assessing liver fibrosis in chronic hepatitis B: a prospective multicentre study," Gut **68**(4), 729–741 (2019).

35. K. He, X. Zhang, and S. Ren, "Deep residual learning for image recognition," *Proceedings of the IEEE Conference on Computer Vision and Pattern Recognition*, 770–778 (2016).

36. C. Szegedy, S. Ioffe, V. Vanhoucke, and A. A. Alemi. "Inception-v4, inception-resnet and the impact of residual connections on learning," arXiv preprint arXiv:1602.07261 (2016).

37. S. Ren, K. He, R. Girshick, and J. Sun, "Faster R-CNN: Towards real-time object detection with region proposal networks," *Advances in neural information processing systems*," 91–99 (2015).

38. A. Conneau, H. Schwenk, L. Barrault, and Y. L. Cun. "Very deep convolutional networks for natural language processing," arXiv preprint arXiv:1606.01781(2016).

39. W. Xiong, J. Droppo, X. Huang, F. Seide, M. Seltzer, A. Stolcke, D. Yu, and G. Zweig. "Achieving human parity in conversational speech recognition," arXiv preprint arXiv:1610.05256(2016).

40. Y. Wang, X. Deng, S. Pu, and Z. Huang. "Residual convolutional CTC networks for automatic speech recognition," arXiv preprint arXiv:1702.07793 (2017).

41. G. Camps-Valls, D. Tuia, L. Bruzzone, and J. A. Benediktsson, "Advances in Hyperspectral Image Classification," IEEE Signal Process. Mag. **31**(1), 45–54 (2014).

42. A. C. Croce and G. Bottiroli, "Autofluorescence spectroscopy and imaging: a tool for biomedical research and diagnosis," Eur. J. Histochem. **58**(4), 2461 (2014).

43. M. Areia, P. Amaro, M. Dinis-Ribeiro, M. A. Cipriano, C. Marinho, A. Costa-Pereira, C. Lopes, L. Moreira-Dias, J. M. Romozinho, H. Gouveia, D. Freitas, and M. C. Leito, "External validation of a classification for methylene blue magnification chromoendoscopy in premalignant gastric lesions," Gastrointest. Endosc. **67**(7), 1011–1018 (2008).

44. J. Zhang, S. B. Guo, and Z. J. Duan, "Application of magnifying narrow-band imaging endoscopy for diagnosis of early gastric cancer and precancerous lesion," BMC Gastroenterol. **11**(1), 135 (2011).

45. O. Dohi, N. Yagi, A. Majima, Y. Horii, T. Kitaichi, Y. Onozawa, K. Suzuki, A. Tomie, R. Kimura-Tsuchiya, T. Tsuji, N. Yamada, N. Bito, T. Okayama, N. Yoshida, K. Kamada, K. Katada, K. Uchiyama, T. Ishikawa, T. Takagi, O. Handa, H. Konishi, Y. Naito, A. Yanagisawa, and Y. Itoh, "Diagnostic ability of magnifying endoscopy with blue laser imaging for early gastric cancer: a prospective study," Gastric Cancer **20**(2), 297–303 (2017).

46. J. A. Evans, B. E. Bouma, J. Bressner, M. Shishkov, G. Y. Lauwers, M. Mino-Kenudson, N. S. Nishioka, and G. J. Tearney, "Identifying intestinal metaplasia at the squamocolumnar junction by using optical coherence tomographyp," Gastrointest. Endosc. **65**(1), 50–56 (2007).

47. X. Zhou, C. Yin, Y. Dang, F. Ye, and G. Zhang, "Identification of the long non-coding RNA H19 in plasma as a novel biomarker for diagnosis of gastric cancer," Sci. Rep. **5**(1), 11516 (2015).

48. Y. Xu, Z. Xu, and X. Ling, "Clinical Study on Gastric Carcinoma and Gastritis Using mid-FT-IR Spectroscopy," Acta Sci. Nat. Univ. Pekin. **43**(4), 441–445 (2007).

49. M. S. Bergholt, W. Zheng, K. Y. Ho, M. Teh, K. G. Yeoh, J. B. Yan So, A. Shabbir, and Z. Huang, "Fiber-optic Raman spectroscopy probes gastric carcinogenesis in vivo at endoscopy," J. Biophotonics **6**(1), 49–59 (2013).